Astronomical Forcing on Loess Deposition in the Junggar Basin Since the Late Pliocene

Zhixiang Wang, Tianfu Zhang, Alexis Licht, Mengmeng Cao, Rui Zhang

Geophysical Research Letters

RESEARCH LETTER
10.1029/2022GL102584

Astronomical Forcing on Loess Deposition in the Junggar Basin Since the Late Pliocene

Zhixiang Wang[1], Tianfu Zhang[2], Alexis Licht[3], Mengmeng Cao[4], and Rui Zhang[5]

[1]Qinghai Provincial Key Laboratory of Geology and Environment of Salt Lakes, Qinghai Institute of Salt Lakes, Chinese Academy of Sciences, Xining, China, [2]Tianjin Center, China Geological Survey, Tianjin, China, [3]CEREGE, Aix Marseille University, CNRS, IRD, INRAE, CEREGE, Aix-en-Provence, France, [4]School of Earth Sciences, China University of Geosciences, Wuhan, China, [5]College of Urban and Environmental Sciences, Hubei Normal University, Huangshi, China

Abstract Deciphering dust outbreak frequency in inland Asia during the late Cenozoic is important for predicting future hydroclimate in the arid parts of China. Here, we present an eolian sedimentary sequence in the southern Junggar Basin over the past 3.5 Ma, Northwestern China. Our data provide a minimum age of 3.5 Ma for the Gurbantunggut Desert. Rb/Sr ratios exhibit prominent 405 Kyr eccentricity cycles throughout our record with weak expression 41 Kyr cycles. We interpret this cyclicity as resulting from a strong impact of the global carbon cycle on western China hydroclimate. By contrast, gamma-ray intensity data displays significant 100- and 41-Kyr cycles after 2.8 Ma, suggesting important variations of the input of westerly derived dust. Our results demonstrate that Westerly derived moisture supply and dust input into inland Asia respond differently to orbital forcing; they suggest that moisture supply and dust transport by the Westerlies are controlled by different drivers since 3.5 Ma.

Plain Language Summary Little is known about how hydrological changes in desert areas respond to today's high atmospheric CO_2 concentrations. Hydroclimatic archives from these areas are critical to understand (and possibly forecast) future hydrological changes at local and regional scales. Herein, we present paleomagnetic, gamma-ray intensity and Rb/Sr data over the past 3.5 Ma from an eolian sedimentary sequence in the southern Junggar Basin, Northwestern China. Our results provide a minimum age of 3.5 Ma for the Gurbantunggut Desert; they show that humidity and Westerlies strength variations in inland Asia follow different cyclicity during the Quaternary, indicating that moisture supply by the Westerlies since 3.5 Ma is not directly impacted by wind strength. Our results show that Junggar hydroclimate is likely poorly sensitive to changes in Westerlies strength, despite their role as moisture conveyor, raising questions about the main control on moisture supply in inland Asia.

Key Points:

- Rb/Sr ratios exhibit prominent 405 Kyr eccentricity cycles throughout our record
- GR data displays significant 100- and 41-Kyr cycles after 2.8 Ma
- Moisture supply by westerlies is not directly impacted by wind strength since at least 3.5 Ma

Supporting Information:

Supporting Information may be found in the online version of this article.

Correspondence to:

Z. Wang and T. Zhang,
wangzhi8905@126.com;
tianfuzhang85@163.com

Citation:

Wang, Z., Zhang, T., Licht, A., Cao, M., & Zhang, R. (2023). Astronomical forcing on loess deposition in the Junggar Basin since the late Pliocene. *Geophysical Research Letters*, *50*, e2022GL102584. https://doi.org/10.1029/2022GL102584

Received 10 FEB 2023
Accepted 6 APR 2023

Author Contributions:

Methodology: Tianfu Zhang, Alexis Licht, Mengmeng Cao, Rui Zhang
Resources: Mengmeng Cao
Software: Tianfu Zhang, Mengmeng Cao, Rui Zhang
Validation: Alexis Licht
Writing – review & editing: Alexis Licht

1. Introduction

Changes in Cenozoic dust flux have a critical impact on atmospheric CO_2 content and deep-sea carbon cycling (Cao et al., 2021). Central Asia and the deserts of western China are an important source of dust, and the pace of their aridification has a strong role on variations of ocean productivity and on the global geochemical cycle (Fang et al., 2020). Therefore, identifying tectonic-and orbital-scale forcing mechanisms of moisture variability in these areas is critical for understanding dust fluxes and global climate (Fang et al., 2020).

During the Holocene, changes in precipitation in western China were not synchronous with those of monsoon humid areas of eastern China (Chen et al., 2016). Late Cenozoic desert expansion and aridification in western China are thus commonly linked to changes in moisture supply by the westerly winds or the Asian summer monsoon, caused by both regional uplift and global cooling (e.g., Fang et al., 2020; Nie et al., 2022; J. Sun et al., 2008). The aridification of wide areas of western China is often attributed to the uplift of the Tianshan Mountains and Pamir Plateau (e.g., Fang et al., 2020), which resulted in a decrease of moisture supply by the Westerlies and regional aridification steps identified at ~26.7–22.6 Ma (Zheng et al., 2015), ~12.2 Ma (Heermance et al., 2018), and ~5.3 Ma (J. Sun et al., 2008). Before the Pliocene, Nie et al. (2022) proposed that Taklimakan Desert greening occurred during Neogene times of Earth's low orbital eccentricity. Frisch et al. (2019) reported that middle Miocene lake level variations in the Ili Basin (southeast Kazakhstan) were significantly controlled by long 405-Kyr eccentricity and obliquity cycles. Late Neogene-Quaternary records show different results. Spectral analysis of grain size data from a loess record at the southern margin of the Taklimakan desert reveals prominent

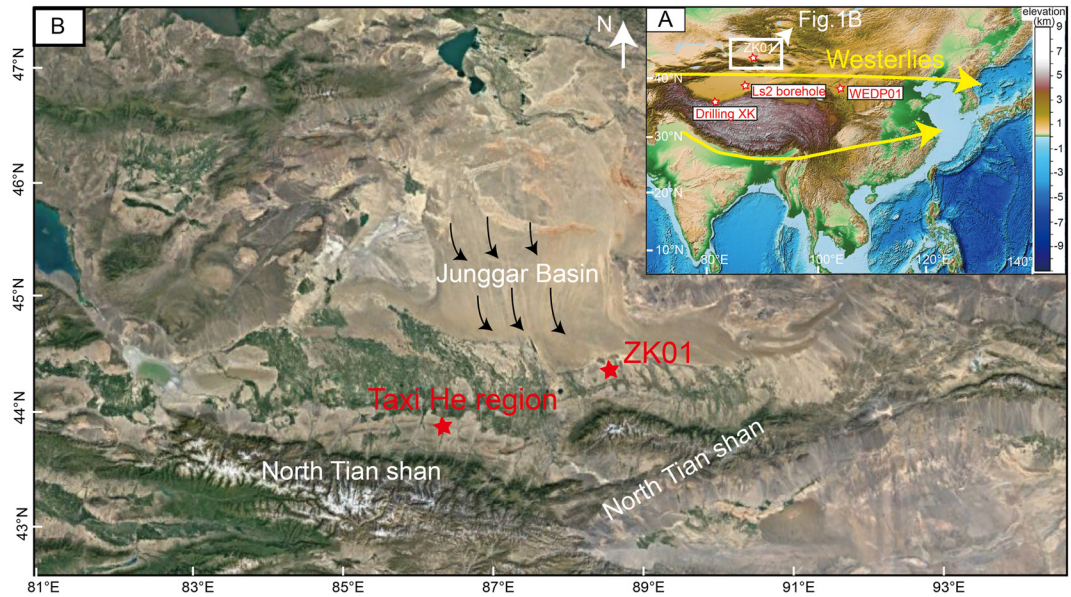

Figure 1. (a) Map showing the location of the ZK01 borehole in the Junggar Basin. The white stars are the locations of sites mentioned in this study. Ls2-W. Liu et al. (2020), Drilling XK-Fang et al. (2020), and WEDP01-C. Liu et al. (2021). The base map was taken from https://www.ngdc.noaa.gov/mgg/global/. (b) Map showing the location of borehole ZK01 and the Taxi He region in the Junggar Basin. The base map was taken from http://www.gditu.net.

41 Kyr cycles from 3.6 to 1.1 Ma, shifting to prominent 100-Kyr cycles after 0.5 Ma (Fang et al., 2020). Magnetic susceptibility for three loess records in the Tianshan Mountains over the past 250 ka also reveals the dominant 100 Kyr cycles (G. Li et al., 2020). These results show that changes in global ice volume likely force the strength of the Westerlies; but the mechanisms driving these astronomical changes in moisture supply are poorly understood.

We recently conducted a drilling study (ZK01 core; 425 m thickness) in the Junggar Basin in the northern foothills of the Tianshan Mountains (Figure 1), downwind of the Gurbantunggut Desert. This paper provides sedimentological-, magneto- and cyclo-stratigraphic data from this core to investigate the orbital sensitivity of aridification in the Gurbantunggut Desert and the mechanisms controlling moisture supply to this part of western China.

2. Geological Context, Materials, and Methods

Today, most of the Junggar Basin area is covered by the Gurbantunggut Desert (48,000 km^2), which is the largest consolidated and semi-consolidated desert in China. The ZK01 core (88.48°E, 44.25°N) is located in the Junggar Basin along the northern foothills of the Tianshan Mountains in the Dishuiyan village, Fukang city in Xinjiang province (Figure 1). The core is 425 m long and is currently stored in the core library of the Dishuiyan village. At present, we know little about the Cenozoic stratigraphic division and its age in the southeastern margin of the Junggar Basin. Most of the research focuses on the Taxi He and Jingou He sections in the southwestern Junggar Basin, which may be due to the relatively complete stratigraphic outlying in these areas. The Cenozoic strata in the Taxi He Section has been divided into Eocene Ziniquanzi Formation, Oligocene Anjihai Formation, Miocene Shawan and Taxihe Formations, Pliocene Dushanzi Formation, and late Pliocene to Pleistocene Xiyu Formation, and its lithology changes from pebbly sandstone and medium-fine sandstones of Eocene to fine-grained lacustrine mudstone of Oligocene and Miocene, and coarse molasse deposits since the latest Miocene (e.g., C. Li et al., 2011). Loess deposits sometimes blanket the landscape at the margin of the desert, and the thickest loess section along the northern foothills of the Tianshan Mountains has been reported to be about 70 m with an age of ~0.8 Ma (Fang et al., 2002), providing a minimum age for the Gurbantunggut Desert. Our borehole is unique (up to 425 m thickness) as it provides a good opportunity to uncover the earliest loess in the Junggar Basin.

Lithologies of the 425-m long core were first described and logged following standard procedures in core logging (Wang et al., 2022). To complete the lithological description of the core, we selected 17 samples between levels

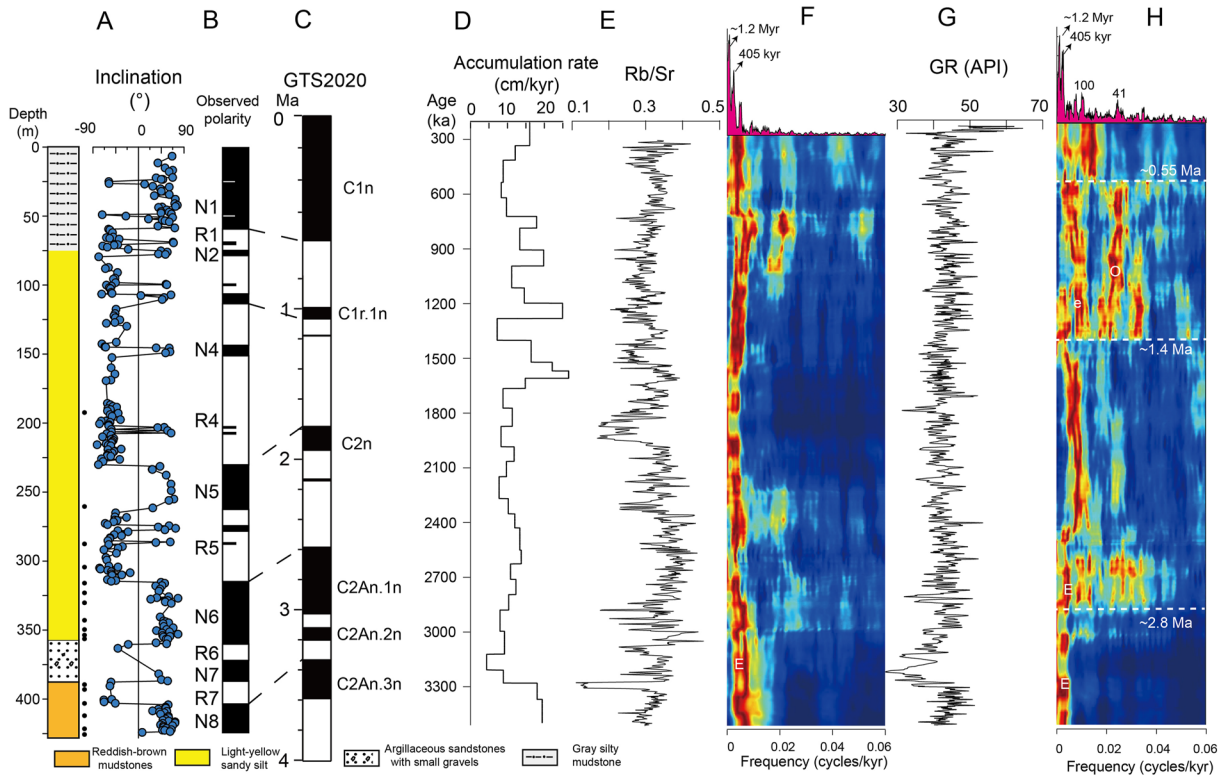

Figure 2. Correlation of the magnetostratigraphy of the ZK01 core (a) and (b) with the GTS2020 (c; Gradstein et al., 2020). (d) The accumulation rate of the ZK01 core with time. (e) Astronomically tuned time series of the Rb/Sr ratio in the ZK01 core. (f) Evolutive Fast Fourier transform spectrum used 600-Kyr sliding window shows periodic variations of the Rb/Sr series with 2π MultiTaper Method power spectrum. (g) The astronomically tuned time series of the GR in the ZK01 core. (h) Evolutive Fast Fourier transform spectrum used 600-Kyr sliding window shows periodic variations of the GR series with 2π MultiTaper Method power spectrum. E-405 Kyr long eccentricity, e-100 Kyr short eccentricity, O-obliquity. The black dots are the sampling spots of grain size.

100 and 425 m for grain size analysis (Figure 2). We selected 2 samples for scanning electron microscope (SEM) analysis of quartz particles at 317 and 415 m, in order to investigate potential marks for aeolian transport of the sediment. We took 300 oriented samples along the core (ca. 1 sample every 1.5 m) for magnetostratigraphic dating. Samples were first air dried and scraped off contaminated surfaces with a knife, and then ground and homogenized in an agate mortar. A total of 1,201 samples were ground into powder and passed through 200-mesh sieve, measured by a portable energy-dispersive Innov-X Systems X-ray fluorescence spectrometer in geochemistry mode using beam 1 (50 kv) and beam 2 (10 kv) to acquire the abundance of rubidium (Rb) and strontium (Sr) at the China University of Geosciences (Wuhan). The continuous GR data were measured using FD-3019 γ logging tool based on EJ/T 611–2005 gamma logging specification through pipes. Detailed preparation, measurement and analysis processes of grain size, SEM, paleomagnetic dating and spectral analysis are provided in Supporting Information S1.

3. Results

3.1. Sedimentary Facies

From bottom to top, the core consists in (Figure 2):

1. From 425 to 385 m: reddish-brown, massive mudstones with no obvious bedding and visible white micrite carbonate crystals and residual plant roots.
2. From 385 to 360 m: argillaceous sandstones with occasional beds of fine gravels (diameter <1 cm).
3. From 360 to 75 m: light-yellowish, loose sandy silt with massive structure, with pores and residual plant roots as well as small micrite carbonate nodules (Figure S1 in Supporting Information S1).
4. From 75 to 0 m: in the upper is gray silty mudstone, massive structure. Fine gravels (diameter <1 cm) occur in some layers.

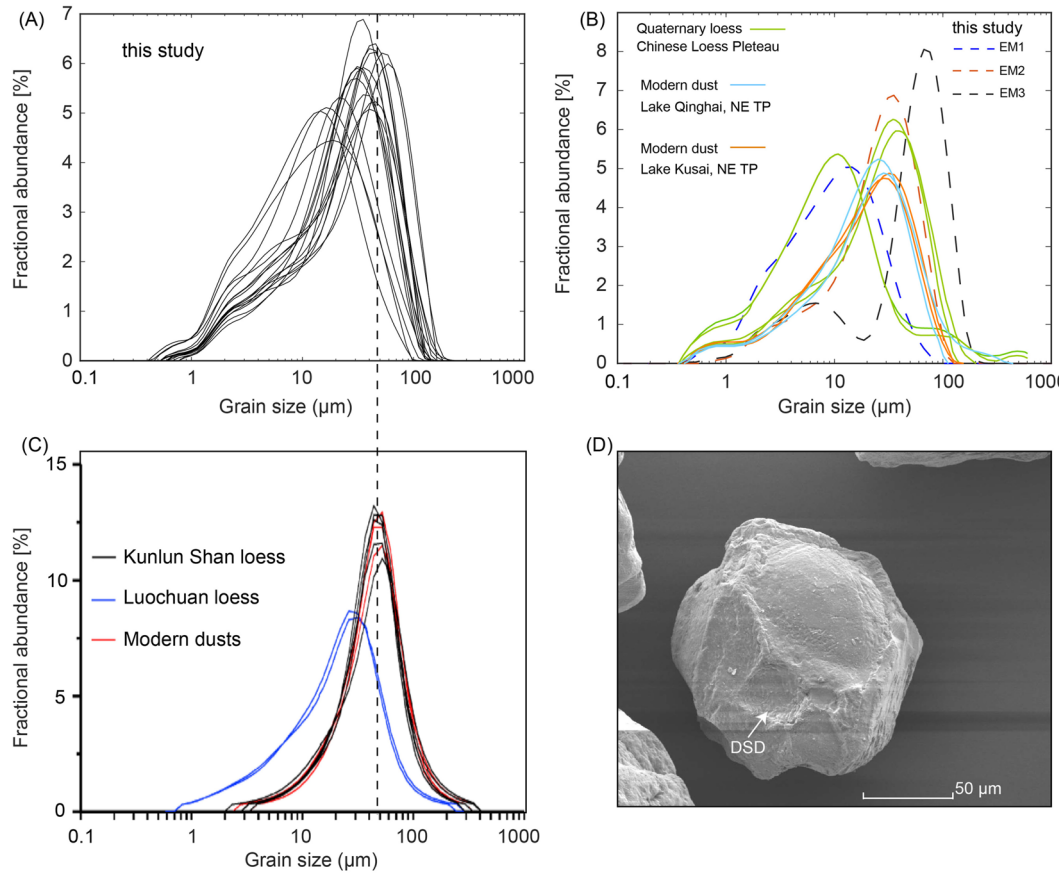

Figure 3. (a) Grain-size frequency distribution curves from the ZK01 core. (b) End members (EM1, EM2, and EM3) of the grain-size data from the ZK01 core (dotted lines) and comparison with grain-size frequency distribution from Quaternary loess in the Chinese Loess Plateau (Vandenberghe et al., 1997), modern dust of the Qinghai (An et al., 2012) and Kusai lakes in the NE Tibet (X. Liu et al., 2009). (c) Aeolian Grain size distribution of representative samples from the Kunlun Shan loess in the Southern Tarim Basin, Luochuan loess in the Chinese Loess Plateau, and modern dust from the Taklimakan Desert (Fang et al., 2020). (d) SEM images of quartz grains at 317 m from the ZK01 core showing morphological features including dish-shaped depressions (DSD).

Sediment from the first (425–385 m) and third (360–75 m) intervals recall aeolian deposits (red clays and loess) with their massive structure, high porosity, carbonate nodules and plant root residues.

The frequency distribution of grain size peaks is mainly concentrated at 30 and 50 μm, similar to the grain size distribution of the Luochuan loess from the Chinese Loess Plateau, modern dust in the Tarim Basin and loess deposits in the West Kunlun Mountains (Figures 3a and 3c). The end-member mode of the ZK01 grain size distribution presents three significant peaks-14.5 μm (EM1), 35.3 μm (EM2), and 66.9 μm (EM3) (Figure 3b). The EM1 and EM2 peaks are consistent with modern dust deposited in the lakes and Quaternary loess from the Tibetan Plateau. The EM3 peak is consistent with the peak of the loess grain size in the West Kunlun Mountains (Figure 3c), suggesting that the EM3 component is mainly derived from detrital material of the nearby deserts.

The scanning electron microscopy of quartz grains with the diameter of ~25–100 μm from the two investigate samples shows obvious dish-shaped and irregular depressions (Figure 3d), features commonly generated by aeolian transport (e.g., Meijer et al., 2020).

3.2. Magnetostratigraphy

Two hundred sixty-four paleomagnetic samples from the ZK01 core provided primary characteristic remanences (ChRM). All data are shown in Figure 2; we identified 9 normal and 8 reversed polarity zones, based on at least three sites per polarity zone. Our preferred correlation to our magnetostratigraphy with the GTS 2020 (Gradstein

et al., 2020) associates polarity zone N1 to chron C1n and polarity zone N8 to chron C2An.3n. This correlation yields accumulation rates of ∼12.78 cm/Kyr for N1-R4, ∼12.72 cm/Kyr for N5-R5, ∼10 cm/Kyr for N6, and ∼13.3 cm/Kyr for R6-R7, respectively. This correlation provides steady accumulation rates, and covers most of the Quaternary (up to 3.5 Ma).

Although our borehole lacks radiogenic or biostratigraphic data, we believe that our acquired age is robust because its magnetostratigraphic correlation with the GTS2020 (Figure 2) yields steady accumulation rates. Sedimentary records from the northwestern Junggar Basin and the Taxihe Section (southwestern Junggar Basin) show predominantly lacustrine deposits before ∼6 Ma, later evolving into alluvial fan sediments (Lu et al., 2013; Niu et al., 2021); this suggests that an age prior to the late Miocene for the ZK01 core is poorly likely, as late Miocene times were regionally more humid (Lu et al., 2013; Niu et al., 2021).

3.3. Spectral Results

The relative content of rubidium (Rb) through time remain relatively stable, with values ranging from 0.002% to 0.01% (Figure S3 in Supporting Information S1). Strontium (Sr) content remains relatively stable in the lower part of the core with values ranging from 0.015% to 0.025%, and then slightly increases in the middle-upper parts, with values reaching 0.03% (Figure S3 in Supporting Information S1). The GR values range from 30 to 70 API, with low values from 360 to 385 m (Figure 2g).

The power spectrum of the GR log series shows significant peaks at ∼45-, 15.8-, 10-, 8.3-, and 4.4-m wavelengths (Figure S4 in Supporting Information S1). Based on the paleomagnetic age constraints and estimated accumulation rates, the 45, 12.5–8.3, and 4.4 m can be assigned to long eccentricity, short eccentricity and obliquity, respectively (Figure 2h). The Rb/Sr series show dominant ∼160 m and 50–45 m wavelengths without significant 16–8 and 4.4 m peaks (Figure S4 in Supporting Information S1). The 50–45 m cycles can be assigned to 405 Kyr cycles (Figure 2f).

Then, we tuned the ∼4.4 m and ∼8.3–12.5 m filter out of the GR series to orbital eccentricity-obliquity of the La2004 (Laskar et al., 2004) based on the paleomagnetic age constraints (Figure S5 in Supporting Information S1), and obtain a duration of 232–3,513 ka astronomical time scale. We use eccentricity-obliquity rather than eccentricity-obliquity-precession composite because precession signal in our records is weak (Figures S4 and S5 in Supporting Information S1). Our age model shows a gap of 0–232 ka (with a thickness of ∼27 m) at the top of the ZK01, that we attribute to (a) partial sampling (0–5 m depth of GR in the upper part were not collected); (b) a large number of soil extraction operations in the 1970s due to building of the local reservoir in the drilling area (Kong & Li, 2012); and (c) glacial water erosion as a result of the disappearance of glaciers in the Tianshan Mountains at the end of Pleistocene (e.g., Takeuchi et al., 2014).

Our results show that GR data are dominated by 405 Kyr cycles before ∼2.8 Ma (Figure 2h and Figure S6 in Supporting Information S1); ∼100 Kyr short eccentricity and obliquity cycles are significantly enhanced between 2.8 and 1.4 Ma (Figure 2h and Figure S6 in Supporting Information S1); the obliquity signal finally strengthens between 1.4 and ∼0.55 Ma (Figure 2h). After ∼0.55 Ma, the 100-Kyr short eccentricity becomes the dominant cyclicity (Figure 2h). The spectral analysis of GR data between 1,100 and 1,300 ka highlights significant 23 Kyr cycles are presented (Figure S8 in Supporting Information S1). By contrast, our Rb/Sr data show monotonic, dominant 405-Kyr cycles with weak 100-Kyr eccentricity, obliquity (41 Kyr) and precession (20 Kyr) cycles in the past 3.5 Ma (Figure 2f). Rb/Sr data tuned to the 400-Kyr eccentricity band show spectral results that are consistent with those from tuned GR data (Figure S9 in Supporting Information S1); these results support our age model for the core. The sampling resolution of our Rb/Sr ratio is ∼2.5 Kyr on average, which is short enough to capture precession signals; the absence of precession, obliquity and short eccentricity in our Rb/Sr ratio is thus not attributed to inadequate sampling resolution.

4. Discussion

4.1. Onset of the Paleo-Gurbantunggut Desert Before 3.5 Ma

Sediment lithology, grain-size, and SEM pictures indicate a prominent aeolian nature for the sediment of intervals 425–385 m and 360–75 m and recall modern loess deposits. These intervals alternate with coarser material, suggesting an environment where aeolian deposition alternate with alluvial fan deposits.

The age of the Gurbantunggut Desert is considered to be at least 0.8 Ma (Fang et al., 2002), whereas the earliest aridification in the Junggar Basin dates back to 24 Ma (J. Sun et al., 2010). Our lithological records show that eolian sediments in the Junggar Basin have been present since at least 3.5 Ma and indicate a paleo-Gurbantunggut Desert since at least this time. This onset of the desert is likely much older, considering the age of the first pieces of evidence for eolian deposition in the Taklimakan desert further south (early to middle Miocene; Heermance et al., 2018; Zheng et al., 2015) or along the Westerly wind pathway further east (middle to upper Eocene; e.g., Licht et al., 2016; Meijer et al., 2021).

4.2. Long Eccentricity Forcing on the Junggar Hydroclimate

Strontium (Sr) is a trace element that substitutes for Ca in the lattices of carbonate minerals and behaves similarly to Ca in many geological processes (Jin et al., 2006). Rubidium (Rb) tends to follow K in silicate minerals because their ionic radius is similar (Chang et al., 2013; Jin et al., 2006). During weathering processes, a relative enrichment of Rb over Sr in parent rocks is expected to occur because Sr has a much higher mobility than the relatively more inert Rb (e.g., Chang et al., 2013; Jin et al., 2006). The behavior of Rb/Sr data has been previously documented in Chinese loess and are associated to the weathering of the aeolian parent material (e.g., An et al., 2001). High Rb/Sr ratios commonly indicate high chemical weathering in response to a relatively warm and humid climate stage, while low Rb/Sr values are associated with colder and drier periods (An et al., 2001). The Rb/Sr ratio can thus be interpreted as a first order proxy for the local hydroclimate.

Rb/Sr data of the ZK01 core show dominant 405 Kyr cycles across the past 3.5 Ma (Figure 2f). This long-eccentricity forcing is similar to what is found in other loess deposits of eastern China covering the same period. Magnetic parameters (χ_{ARM}/SIRM) of the borehole WEDP01 in the Tengger Desert over the past 3 Ma, which have been interpreted as a proxy of wet-dry variability, also display a dominant 405-Kyr eccentricity signal (C. Liu et al., 2021) as well as $\delta^{13}C_{carb}$ data from the Ls2 borehole in the eastern Tarim Basin, interpreted as reflecting regional vegetation cover and biological productivity (W. Liu et al., 2020; location of both cores on Figure 1). Prominent eccentricity cycles are also recognized in hydrological records from the late Oligocene to early Miocene fluviolacustrine sediments in the Lanzhou Basin, NE Tibet (Ao et al., 2021; Wang et al., 2020), late Miocene fluviolacustrine sequence in the Qaidam Basin, NE Tibet (Nie et al., 2017), and Pliocene lacustrine records in the Weihe Basin, North China (Zhang et al., 2022). Thus, eccentricity forcing hydrological variability was a widespread phenomenon of Asian monsoon regions during unipolar icehouse periods (Ao et al., 2021; Zhang et al., 2022). In non-monsoonal Central Asia, sedimentary records during late Miocene to Quaternary period also show that hydrological cycles are significantly controlled by eccentricity cycles (e.g., Fang et al., 2020; Frisch et al., 2019; W. Liu et al., 2014; Nie et al., 2022).

Explaining the dominance of 405 Kyr cycles in our hydroclimate record is not straightforward, as summer insolation at this latitude should be dominated by precession forcing (e.g., Laskar et al., 2004). Paleoclimatic records from the late Miocene strata of the northwestern Tarim Basin, Western China, show wetter conditions during times of eccentricity minima (Nie et al., 2022). Nie et al. (2022) proposed that decreased penetration of monsoonal moisture into East Asia during eccentricity minima allowed an increased supply of monsoonal-derived moisture to western China. In this sense, the dominance of 405 Kyr cycles might anti-correlate with the 405 Kyr cycles seen in some monsoonal records in eastern China.

Climatic simulations have suggested that 405-Kyr eccentricity cycles have a strong influence on the long-term carbon cycle over the past 35 Ma (de Boer et al., 2014). In the meantime, a modulation of precession-dominated 65°N summer insolation by the eccentricity may impact chemical weathering in the Asian mainland (e.g., Ao et al., 2021; C. Liu et al., 2021). The strong 405-Kyr signal in our Rb/Sr ratios, as well as in other regional records, may also result from both influences, with eccentricity modulation of the summer insolation being amplified through nonlinear interactions with the long-term global carbon cycle (e.g., Ao et al., 2021; de Boer et al., 2014; Guo et al., 2022).

4.3. Astronomical Forcing of Westerly Winds Dynamics

The gamma-ray intensity (GR) in sediments reflects potassium (K), uranium (U), and thorium (Th) content (e.g., Schnyder et al., 2006). K is common in many minerals such as clays, feldspar, and mica. U and Th are concentrated in a number of sedimentary host minerals including clays, feldspar, heavy minerals, and phosphate,

and U is often concentrated in organic matter (Schnyder et al., 2006). High GR values are generally attributed to clay-rich sediments, whereas lower GR values are associated with coarser-grained sediments (e.g., Vaucher et al., 2023; Wang et al., 2022). Provenance changes, sediment supply, chemical weathering and wind strength have significant effects on GR data (e.g., Schnyder et al., 2006; Vaucher et al., 2023; Wang et al., 2022). In general, eolian deposits in the ZK01 core are associated with higher GR values, and sandstone with lower values (<40 API within the 360–385 m; Figure 2g). Interestingly, we only found a poor correlation between grain size and GR data for the 17 samples for which we acquired grain-size data (correlation coefficient = 0.47; Table S1 in Supporting Information S1); most of these samples come from the 3.5–2.8 Ma interval (10 out of 17).

Our GR spectral record displays four main stages: (a) 3.5–2.8 Ma, where GR cyclicity is dominated by 405-Kyr long-eccentricity cycles; (b) 2.8–1.4 Ma, with appearance of short-eccentricity and obliquity cycles; and (c) 1.4–0.55 Ma, with a significant increase in obliquity signal; (d) 0.55–0.3 Ma, when the obliquity signal significantly decreases (Figure 2h).

The prominence of 405-Kyr long-eccentricity cycles during the 3.5–2.8 Ma time window is similar to what is seen in our Rb/Sr record. This time-window precedes the early Quaternary boost in loess accumulation in eastern China (e.g., Y. Sun et al., 2010). Sediment of this time window includes a significant part of coarser material attributed to alluvial fan material (levels 385–360 m), and includes the lowest accumulation rates of our record (Figure 2d). These observations suggest lower aeolian input during 3.3–2.8 Ma interval window, combined with an increase of alluvial fan activity. We postulate that our GR data are likely more impacted by variations of pedogenic intensity and facies changes rather than variations of dust input by the Westerlies during this time window; this explanation is supported by the lack of correlation between grain size and GR data. The coarser interval 385-360 m corresponds to the mid Pliocene Warm Period, characterized by sub-modern pCO_2 (~400 ppm), with average global warming of 2–3°C (Burke et al., 2018; Pagani et al., 2010). We suggest that higher global CO_2 concentrations of the mid Pliocene Warm Period might have led to an intensification of the regional hydrological cycle, with heavier rainfall resulting in a decrease in dust generation and a reactivation of Miocene alluvial fan systems.

After ~2.8 Ma, the GR data changed from the dominant 405 Kyr eccentricity cycles into combined 100 Kyr eccentricity and 41 Kyr obliquity control (Figure 2h). This forcing is similar to what is seen in the hematite/goethite record from ODP 1143 in the South China Sea (Ao et al., 2011), K (wt.%) record from the IODP U1422 in the Japan Sea (Cao et al., 2021), and quartz grain size from the Lingtai Section in the Chinese Loess Plateau (Y. Sun et al., 2010). We suggest that this turn-over period is a consequence of the influence of Northern Hemisphere ice sheet expansion on the regional water cycle (e.g., Cao et al., 2021; Y. Sun et al., 2010) and the onset of a strong imprint of Westerlies strength variation on our record. Westerlies strength has been proposed to be mainly influenced by expansion of Northern Hemisphere ice sheets (e.g., Fang et al., 2020). Therefore, occurrence of 41 Kyr cyclicity in our GR record indicates the onset of a significant influence of the Northern Hemispheric ice sheets on arid Central Asia.

The increase of obliquity signal starting at 1.4 Ma is also found in Pacific dust flux, $\delta^{13}C_{benthic}$ and $\delta^{18}O_{benthic}$ data (Cao et al., 2021), suggesting that this change of orbital sensitivity is regional. Following Cao et al. (2021), we postulate that this increase of obliquity signal could be attributed to a threshold in Arctic ice-sheet expansion (e.g., Cao et al., 2021; Reinardy et al., 2018), leading to increased sensitivity of the Earth's oceanic-atmospheric systems to high-latitude 41 Kyr obliquity variability (e.g., Cao et al., 2021; Reinardy et al., 2018). Well-marked 23 Kyr cycles are also ephemerally present in GR data between 1,100 and 1,300 ka (Figure S8 in Supporting Information S1), which suggests that precession altered our GR values via the modulation of middle-latitude insolation. After ~0.55 Ma, obliquity signal weakened and turned into the 100-Kyr cycle control, in line with the loess record from the Tarim Basin (Figure 2h; Fang et al., 2020).

Taken together, our results thus demonstrate that GR data at orbital time scale are strongly affected by high-latitude ice volume after 2.8 Ma. The driver of GR variation in our record remains yet to be clearly identified, as the correlation between grain-size and GR data is not particularly well-marked. Cyclic changes of dust provenance (and dust mineralogy) could additionally explain some of the observed variations. This potential forcing is yet difficult to identify based solely on GR and elemental data, and calls for a more detailed study of dust mineralogy and provenance in the Gurbantunggut Desert.

5. Conclusion

In this study, we provide a ~3.3-Myr-long high-resolution GR and Rb/Sr records to decipher orbital-scale wet-dry variability in the Central arid region during the late Pliocene to Pleistocene period. Our Rb/Sr ratios display

dominant 405 Kyr cycles throughout the past 3.5 Ma, suggesting that westerly derived moisture is strongly impact by the global carbon cycle at the orbital scale. Our GR data display a similar signal before a turnover event at 2.8 Ma when 405-, 100-, and 41-Kyr cycles become more important. We postulate that this event reflects a significant increase of high-latitude ice volume. Our results demonstrate that dry-wet changes and Westerlies dynamics in inland Asia follow different cyclicity during the Quaternary, indicating that moisture supply by the Westerlies is not directly impacted by wind strength. Our data also provide a minimum age of 3.5 Ma for the Gurbantunggut Desert of the Junggar Basin.

Data Availability Statement

All of our measured proxy data (including GR, Rb/Sr ratios and Paleomagnetic data) presented here available in the figshare website (available from https://figshare.com/s/d81f4b43ee3b46d9bdb1).

Acknowledgments
We thank Yuqi Xu for her assistance with field sampling. We are grateful to associate Editor and two reviewers for their constructive reviews of this paper. This work was supported by Hubei Province Post-Doctoral Innovation Research Station (1232002) and the China Postdoctoral Foundation (2020M682517). Rui Zhang thanks the support of SKLLQG2227 (State Key Laboratory of Loess and Quaternary Geology, Institute of Earth Environment, CAS).

References

An, Z., Colman, S. M., Zhou, W., Li, X., Brown, E. T., Jull, A. J., et al. (2012). Interplay between the Westerlies and Asian monsoon recorded in Lake Qinghai sediments since 32 ka. *Scientific Reports*, *2*, 1–7. https://doi.org/10.1038/srep00619

An, Z., Kutzbach, J. E., Prell, W. L., & Porter, S. C. (2001). Evolution of Asian monsoons and phased uplift of the Himalaya-Tibetan plateau since late Miocene times. *Nature*, *411*(6833), 62–66. https://doi.org/10.1038/35075035

Ao, H., Dekkers, M. J., Qin, L., & Xiao, G. (2011). An updated astronomical timescale for the Plio-Pleistocene deposits from South China Sea and new insights into Asian monsoon evolution. *Quaternary Science Reviews*, *30*(13–14), 1560–1575. https://doi.org/10.1016/j.quascirev.2011.04.009

Ao, H., Liebrand, D., Dekkers, M. J., Zhang, P., Song, Y., Liu, Q., et al. (2021). Eccentricity-paced monsoon variability on the northeastern Tibetan Plateau in the late Oligocene high CO_2 world. *Science Advances*, *7*(51), eabk2318. https://doi.org/10.1126/sciadv.abk2318

Burke, K. D., Williams, J. W., Chandler, M. A., Haywood, A. M., Lunt, D. J., & Otto-Bliesner, B. L. (2018). Pliocene and Eocene provide best analogs for near-future climates. *Proceedings of the National Academy of Sciences of the United States of America*, *115*(52), 13288–13293. https://doi.org/10.1073/pnas.1809600115

Cao, M., Wang, Z., Sui, Y., Li, Y., Zhang, Z., Xiao, A., et al. (2021). Mineral dust coupled with climate-carbon cycle on orbital timescales over the past 4 Ma. *Geophysical Research Letters*, *48*(18), e2021GL095327. https://doi.org/10.1029/2021gl095327

Chang, H., An, Z., Wu, F., Jin, Z., Liu, W., & Song, Y. (2013). A Rb/Sr record of the weathering response to environmental changes in westerly winds across the Tarim Basin in the late Miocene to the early Pleistocene. *Palaeogeography, Palaeoclimatology, Palaeoecology*, *386*, 364–373. https://doi.org/10.1016/j.palaeo.2013.06.006

Chen, F., Jia, J., Chen, J., Li, G., Zhang, X., Xie, H., et al. (2016). A persistent Holocene wetting trend in arid central Asia, with wettest conditions in the late Holocene, revealed by multi-proxy analyses of loess-paleosol sequences in Xinjiang, China. *Quaternary Science Reviews*, *146*, 134–146. https://doi.org/10.1016/j.quascirev.2016.06.002

de Boer, B., Lourens, L. J., & Wal, R. S. W. V. D. (2014). Persistent 400,000-year variability of Antarctic ice volume and the carbon cycle is revealed throughout the Plio-Pleistocene. *Nature Communications*, *5*(1), 2999. https://doi.org/10.1038/ncomms3999

Fang, X., An, Z., Clemens, S. C., Zan, J., Shi, Z., Yang, S., & Han, W. (2020). The 3.6-Ma aridity and westerlies history over midlatitude Asia linked with global climatic cooling. *Proceedings of the National Academy of Sciences of the United States of America*, *117*(40), 24729–24734. https://doi.org/10.1073/pnas.1922710117

Fang, X., Shi, Z., Yang, S., Yan, M., Li, J., & Jiang, P. A. (2002). Loess in the Tian Shan and its implications for the development of the Gurbantunggut Desert and drying of northern Xinjiang. *Chinese Science Bulletin*, *47*(16), 1381–1387. https://doi.org/10.1360/02tb9305

Frisch, K., Voigt, S., Verestek, V., Appel, E., Albert, R., Gerdes, A., et al. (2019). Long-period astronomical forcing of westerlies' strength in central Asia during Miocene climate cooling. *Paleoceanography and Paleoclimatology*, *34*, 1784–1806. https://doi.org/10.1029/2019PA003642

Gradstein, F. M., Ogg, J. G., Schmitz, M., & Ogg, G. (2020). *The geologic time scale 2020*. Elsevier.

Guo, B., Nie, J., Li, J., Xiao, W., & Pan, F. (2022). Expansion/shrinkage history of the Paratethys Sea during the Eocene: New insights from eolian Red Clay records in the Altyn Mountains, northern China. *Frontiers of Earth Science*, *10*. https://doi.org/10.3389/feart.2022.1052627

Heermance, R. V., Pearson, J., Moe, A., Langtao, L., Jianhong, X., Jie, C., et al. (2018). Erg deposition and development of the ancestral Taklimakan Desert (western China) between 12.2 and 7.0 Ma. *Geology*, *46*(10), 919–922. https://doi.org/10.1130/g45085.1

Jin, Z., Cao, J., Wu, J., & Wang, S. (2006). A Rb/Sr record of catchment weathering response to Holocene climate change in Inner Mongolia. *Earth Surface Processes and Landforms*, *31*(3), 285–291. https://doi.org/10.1002/esp.1243

Kong, Q. X., & Li, W. C. (2012). Reinforcement engineering design of Xidalongkou reservoir in Jimsar Country, Xinjiang. *Water Conservancy Science and Technology and Economy*, *18*(12), 42–43. (In Chinese).

Laskar, J., Robutel, P., Joutel, F., Gastineau, M., Correia, A., & Levrard, B. (2004). A long-term numerical solution for the insolation quantities of the Earth. *Astronomy & Astrophysics*, *428*(1), 261–285. https://doi.org/10.1051/0004-6361:20041335

Li, C., Dupont-Nivet, G., & Guo, Z. (2011). Magnetostratigraphy of the northern Tian Shan foreland, Taxi He section, China. *Basin Research*, *23*(1), 101–117. https://doi.org/10.1111/j.1365-2117.2010.00475.x

Li, G., Yang, H., Stevens, T., Zhang, X., Zhang, H., Wei, H., et al. (2020). Differential ice volume and orbital modulation of quaternary moisture patterns between Central and East Asia. *Earth and Planetary Science Letters*, *530*, 115901. https://doi.org/10.1016/j.epsl.2019.115901

Licht, A., Dupont-Nivet, G., Pullen, A., Kapp, P., Abels, H. A., Lai, Z., et al. (2016). Resilience of the Asian atmospheric circulation shown by Paleogene dust provenance. *Nature Communications*, *7*(1), 12390. https://doi.org/10.1038/ncomms12390

Liu, C., Nie, J., Li, Z., Qiao, Q., Abell, J. T., Wang, F., & Xiao, W. (2021). Eccentricity forcing of East Asian monsoonal systems over the past 3 million years. *Proceedings of the National Academy of Sciences of the United States of America*, *118*(43). https://doi.org/10.1073/pnas.2107055118

Liu, W., Liu, Z., An, Z., Sun, J., Chang, H., Wang, N., et al. (2014). Late Miocene episodic lakes in the arid Tarim Basin, western China. *Proceedings of the National Academy of Sciences of the United States of America*, *111*(46), 16292–16296. https://doi.org/10.1073/pnas.1410890111

Liu, W., Liu, Z., Sun, J., Song, C., Chang, H., Wang, H., et al. (2020). Onset of permanent Taklimakan Desert linked to the mid-Pleistocene transition. *Geology*, *48*(8), 782–786. https://doi.org/10.1130/g47406.1

Liu, X., Dong, H., Yang, X., Herzschuh, U., Zhang, E., Stuut, J.-B. W., & Wang, Y. (2009). Late Holocene forcing of the Asian winter and summer monsoon as evidenced by proxy records from the northern Qinghai–Tibetan Plateau. *Earth and Planetary Science Letters*, *280*(1–4), 276–284. https://doi.org/10.1016/j.epsl.2009.01.041

Lu, H., Zhang, W., Li, Y., Dong, C., Zhang, T., Zhou, Z., & Zheng, X. (2013). Rock magnetic properties and paleoenvironmental implications of an 8-Ma Late Cenozoic terrigenous succession from the northern Tian Shan foreland basin, northwestern China. *Global and Planetary Change*, *111*, 43–56. https://doi.org/10.1016/j.gloplacha.2013.08.007

Meijer, N., Dupont-Nivet, G., Barbolini, N., Woutersen, A., Rohrmann, A., Zhang, Y., et al. (2021). Loess-like dust appearance at 40 Ma in central China. *Paleoceanography and Paleoclimatology*, *36*(3), e2020PA003993. https://doi.org/10.1029/2020pa003993

Meijer, N., Dupont-Nivet, G., Licht, A., Trabucho-Alexandre, J., Bourquin, S., & Abels, H. A. (2020). Identifying eolian dust in the geological record. *Earth-Science Reviews*, *211*, 103410. https://doi.org/10.1016/j.earscirev.2020.103410

Nie, J., Garzione, C., Su, Q., Liu, Q., Zhang, R., Heslop, D., et al. (2017). Dominant 100,000-year precipitation cyclicity in a late Miocene lake from northeast Tibet. *Science Advances*, *3*(3), e1600762. https://doi.org/10.1126/sciadv.1600762

Nie, J., Wang, W., Heermance, R., Gao, P., Xing, L., Zhang, X., et al. (2022). Late Miocene Tarim desert wetting linked with eccentricity minimum and East Asian monsoon weakening. *Nature Communications*, *13*(1), 3977. https://doi.org/10.1038/s41467-022-31577-w

Niu, G., Li, X., Zhao, Y., Yang, F., Li, S., & Wan, Z. (2021). Magnetostratigraphy of a drilling core from the Baiyanghe alluvial fan at the western margin of the Junggar Basin, NW China and its paleoenvironmental significance. *Quaternary International*, *589*, 1–11. https://doi.org/10.1016/j.quaint.2021.02.016

Pagani, M., Liu, Z., LaRiviere, J., & Ravelo, A. C. (2010). High Earth-system climate sensitivity determined from Pliocene carbon dioxide concentrations. *Nature Geoscience*, *3*(1), 27–30. https://doi.org/10.1038/ngeo724

Reinardy, B. T., Sejrup, H. P., Hjelstuen, B. O., King, E., & Augedal, H. (2018). A Quaternary aminostratigraphy constraining chronology of depositional environments in the North Sea Basin. *Marine Geology*, *402*, 139–152. https://doi.org/10.1016/j.margeo.2017.11.004

Schnyder, J., Ruffell, A., Deconinck, J.-F., & Baudin, F. (2006). Conjunctive use of spectral gamma-ray logs and clay mineralogy in defining late Jurassic–early Cretaceous palaeoclimate change (Dorset, UK). *Palaeogeography, Palaeoclimatology, Palaeoecology*, *229*(4), 303–320. https://doi.org/10.1016/j.palaeo.2005.06.027

Sun, J., Ye, J., Wu, W., Ni, X., Bi, S., Zhang, Z., et al. (2010). Late Oligocene–Miocene mid-latitude aridification and wind patterns in the Asian interior. *Geology*, *38*(6), 515–518. https://doi.org/10.1130/g30776.1

Sun, J., Zhang, L., Deng, C., & Zhu, R. (2008). Evidence for enhanced aridity in the Tarim Basin of China since 5.3Ma. *Quaternary Science Reviews*, *27*(9–10), 1012–1023. https://doi.org/10.1016/j.quascirev.2008.01.011

Sun, Y., An, Z., Clemens, S. C., Bloemendal, J., & Vandenberghe, J. (2010). Seven million years of wind and precipitation variability on the Chinese Loess Plateau. *Earth and Planetary Science Letters*, *297*(3–4), 525–535. https://doi.org/10.1016/j.epsl.2010.07.004

Takeuchi, N., Fujita, K., Aizen, V. B., Narama, C., Yokoyama, Y., Okamoto, S., et al. (2014). The disappearance of glaciers in the Tien Shan mountains in central Asia at the end of Pleistocene. *Quaternary Science Reviews*, *103*, 26–33. https://doi.org/10.1016/j.quascirev.2014.09.006

Vandenberghe, J., Zhisheng, A., Nugteren, G., Huayu, L., & Van Huissteden, K. (1997). New absolute time scale for the quaternary climate in the Chinese loess region by grain-size analysis. *Geology*, *25*(1), 35–38. https://doi.org/10.1130/0091-7613(1997)025<0035:natsft>2.3.co;2

Vaucher, R., Zeeden, C., Hsieh, A. I., Kaboth-Bahr, S., Lin, A. T., Horng, C.-S., & Dashtgard, S. E. (2023). Hydroclimate dynamics during the Plio-Pleistocene transition in the northwest Pacific realm. *Global and Planetary Change*, *223*, 104088. https://doi.org/10.1016/j.gloplacha.2023.104088

Wang, Z., Mao, Y., Geng, J., Huang, C., Ogg, J., Kemp, D. B., et al. (2022). Pliocene-Pleistocene evolution of the lower Yellow River in eastern North China: Constraints on the age of the Sanmen Gorge connection. *Global and Planetary Change*, *213*, 103835. https://doi.org/10.1016/j.gloplacha.2022.103835

Wang, Z., Zhang, Z., Huang, C., Shen, J., Sui, Y., & Qian, Z. (2020). Astronomical forcing of lake evolution in the Lanzhou Basin during early Miocene period. *Earth and Planetary Science Letters*, *554*, 116648. https://doi.org/10.1016/j.epsl.2020.116648

Zhang, Z., Licht, A., De Vleeschouwer, D., Wang, Z., Li, Y., Kemp, D. B., et al. (2022). East Asian monsoonal climate sensitivity changed in the late Pliocene in response to Northern Hemisphere glaciations. *Geophysical Research Letters*, *49*(23), e2022GL101280. https://doi.org/10.1029/2022gl101280

Zheng, H., Wei, X., Tada, R., Clift, P. D., Wang, B., Jourdan, F., et al. (2015). Late Oligocene-early Miocene birth of the Taklimakan Desert. *Proceedings of the National Academy of Sciences of the United States of America*, *112*(25), 7662–7667. https://doi.org/10.1073/pnas.1424487112

References From the Supporting Information

Ghil, M., Allen, M., Dettinger, M., Ide, K., Kondrashov, D., Mann, M., et al. (2002). Advanced spectral methods for climatic time series. *Reviews of Geophysics*, *40*(1), 3-1–3-41. https://doi.org/10.1029/2000rg000092

Jones, C. H. (2002). User-driven integrated software lives: "Paleomag" paleomagnetics analysis on the Macintosh. *Computers & Geosciences*, *28*(10), 1145–1151. https://doi.org/10.1016/s0098-3004(02)00032-8

Kodama, K. P., & Hinnov, L. A. (2014). *Rock magnetic cyclostratigraphy*. John Wiley & Sons.

Li, Z., Sun, D., Chen, F., Wang, F., Zhang, Y., Guo, F., et al. (2014). Chronology and paleoenvironmental records of a drill core in the central Tengger Desert of China. *Quaternary Science Reviews*, *85*, 85–98. https://doi.org/10.1016/j.quascirev.2013.12.003

Lisiecki, L. E., & Raymo, M. E. (2005). A Pliocene-Pleistocene stack of 57 globally distributed benthic $\delta^{18}O$ records. *Paleoceanography*, *20*(1). https://doi.org/10.1029/2004pa001071

Mann, M. E., & Lees, J. M. (1996). Robust estimation of background noise and signal detection in climatic time series. *Climatic Change*, *33*(3), 409–445. https://doi.org/10.1007/bf00142586

Paillard, D., Labeyrie, L., & Yiou, P. (1996). Macintosh program performs time-series analysis. *Eos, Transactions American Geophysical Union*, *77*(39), 379. https://doi.org/10.1029/96eo00259

Westerhold, T., Marwan, N., Drury, A. J., Liebrand, D., Agnini, C., Anagnostou, E., et al. (2020). An astronomically dated record of Earth's climate and its predictability over the last 66 million years. *Science*, *369*(6509), 1383–1387. https://doi.org/10.1126/science.aba6853